A&A 490, 873–877 (2008)
DOI: 10.1051/0004-6361:200810239

Astronomy & Astrophysics

A 3D radiative transfer framework

III. Periodic boundary conditions

P. H. Hauschildt[1] and E. Baron[1,2,3]

[1] Hamburger Sternwarte, Gojenbergsweg 112, 21029 Hamburg, Germany
e-mail: yeti@hs.uni-hamburg.de
[2] Dept. of Physics and Astronomy, University of Oklahoma, 440 W. Brooks, Rm 100, Norman, OK 73019, USA
e-mail: baron@ou.edu
[3] Computational Research Division, Lawrence Berkeley National Laboratory, MS 50F-1650, 1 Cyclotron Rd, Berkeley, CA 94720-8139, USA

Received 22 May 2008 / Accepted 24 July 2008

ABSTRACT

Aims. We present a general method to solve radiative transfer problems including scattering in the continuum as well as in lines in 3D configurations with periodic boundary conditions.

Methods. The scattering problem for line transfer is solved via means of an operator splitting (OS) technique. The formal solution is based on a full characteristics method. The approximate Λ operator is constructed considering nearest neighbors exactly. The code is parallelized over both wavelength and solid angle using the MPI library.

Results. We present the results of several test cases with different values of the thermalization parameter and two choices for the temperature structure. The results are directly compared to 1D plane parallel tests. The 3D results agree very well with the well-tested 1D calculations.

Conclusions. Advances in modern computers will make realistic 3D radiative transfer calculations possible in the near future. Our current code scales to very large numbers of processors, but requires larger memory per processor at high spatial resolution.

Key words. radiative transfer – scattering

1. Introduction

Interest in 3-D radiative transfer in stellar atmospheres has grown with the calculations of Asplund and collaborators (Asplund et al. 1999, 2000; Asplund 2000; Asplund et al. 2005; Grevesse et al. 2007). This work has indicated that the solar oxygen abundance needs to be revised downward. However, the revised abundances are difficult to reconcile with helioseismological results (see Basu & Antia 2008, and references therein). The work of Asplund et al. is based on comparisons of synthetic spectra produced by formal solutions of hydrodynamical models of solar convection. We present a framework for solving the full scattering problem that is applicable to hydrodynamical calculations of stellar atmospheres. Hauschildt & Baron (2006, hereafter Paper I) and Baron & Hauschildt (2007, hereafter Paper II) described a framework for the solution of the radiative transfer equation for scattering continua and lines in 3D (when we say 3D we mean three spatial dimensions, plus three momentum dimensions) for the time independent, static case. In the 3rd paper of this series we apply these methods to problems with period boundary conditions which typically arise in radiation-hydrodynamical simulations of convective atmospheres. In such calculations the radiation transport has to be simplified compared to the full problem in order to keep the calculations tractable. However, a full solution of the scattering line problem is needed for comparison and post-processing of the structures.

We describe our method, its rate of convergence, and present comparisons to our well-tested 1-D calculations.

2. Method

In the following discussion we use notation of Papers I and II. The basic framework and the methods used for the formal solution and the solution of the scattering problem via operator splitting are discussed in detail in Papers I and II and will thus not be repeated here.

In the following we assume (without restriction) that we have periodic boundary conditions in the x and y coordinates, and for the z coordinate that the "bottom" (large optical depth) is at $z = z_{\rm min}$ and the "top" (interface to empty space) is at $z = z_{\rm max}$. The implementation of the periodic boundary conditions within our framework is simple: we use a "full characteristics" approach that completely tracks a set of characteristics of the radiative transfer equation from the outer boundary through the computational domain to their exit voxel and takes care that each voxel is hit by at least one characteristic per solid angle. One characteristic is started on each boundary voxel (in this case these are the planes $z = z_{\rm min}$ and $z = z_{\rm max}$) and then tracked until it leaves the other boundary. The direction of a bundle of full characteristics is determined by a set of solid angles (θ, φ) which correspond to a normalized momentum space vector (p_x, p_y, p_z). The periodic boundary conditions are simply implemented as a wrap-around (e.g., passing $x_{\rm max}$ for $p_x > 0$ wraps around to $x_{\rm min}$) and continuing of the characteristic until it leaves at the z boundary. Characteristics with very small $|p_z|$ would require a large number of wrap-arounds (and eventually would lead to infinitely long characteristics), therefore, we limit the number of wrap-arounds per voxel to a prescribed value, typically around 16

Article published by EDP Sciences

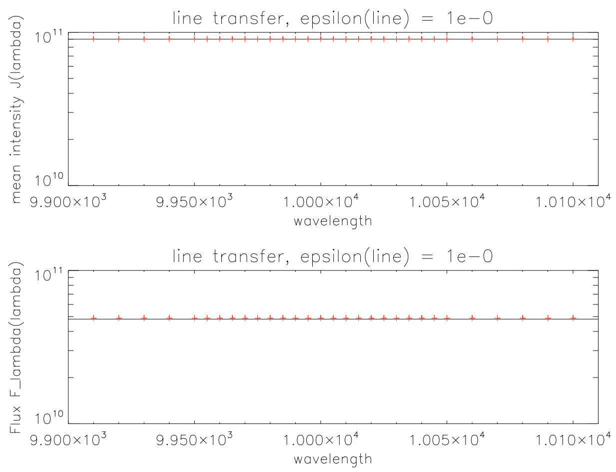

Fig. 1. The mean intensity J and the z component of the radiation flux F at $\tau_{\rm std} = 0$ as function of wavelength. The + symbols are the comparison results with the 1D solver, the full lines the results from the 3D PBC solution. The results are for $\epsilon_l = 1$ and constant temperatures.

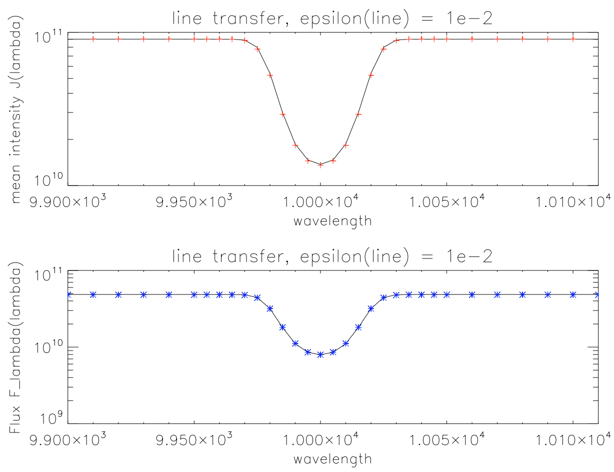

Fig. 2. The mean intensity J and the z component of the radiation flux F at $\tau_{\rm std} = 0$ as function of wavelength. The + symbols are the comparison results with the 1D solver, the full lines the results from the 3D PBC solution. The results are for $\epsilon_l = 10^{-2}$ and constant temperatures.

(tests have shown that larger values do not affect the results, values as small as 4 are usable in plane-parallel tests). The code is parallelized as described in Paper II.

3. Plane-parallel tests

3.1. Testing environment

We use the framework discussed in Papers I and II as the baseline for the line transfer problems discussed in this paper. Our basic setup is similar to that discussed in Paper II. Periodic boundary conditions (PBCs) are realized in a plane parallel slab. We use PBCs on the x and y axes, $z_{\max}$ is at the outside boundary, $z_{\min}$ the inside boundary. The slab has a finite optical depth in the z axis. The grey continuum opacity is parameterized by a power law in the continuum optical depth $\tau_{\rm std}$ in the z axis. The basic model parameters are

1. thickness of the slab, $z_{\max} - z_{\min} = 10^7$ cm;
2. minimum optical depth in the continuum, $\tau_{\rm std}^{\min} = 10^{-8}$ and maximum optical depth in the continuum, $\tau_{\rm std}^{\max} = 10$;
3. constant temperatures (in all axes), $T = 10^4$ K;
4. outer boundary condition, $I_{\rm bc}^{-} \equiv 0$ and diffusion inner boundary condition for all wavelengths;
5. parameterized coherent & isotropic continuum scattering by defining

   $$\chi_{\rm c} = \epsilon_{\rm c}\kappa_{\rm c} + (1 - \epsilon_{\rm c})\sigma_{\rm c}$$

   with $0 \le \epsilon_{\rm c} \le 1$. $\kappa_{\rm c}$ and $\sigma_{\rm c}$ are the continuum absorption and scattering coefficients.

The line of the simple 2-level model atom is parameterized by the ratio of the profile averaged line opacity χ_l to the continuum opacity $\chi_{\rm c}$ and the line thermalization parameter ϵ_l. For the test cases presented below, we have used $\epsilon_{\rm c} = 1$ and a constant temperature and thus a constant thermal part of the source function for simplicity (and to save computing time) and set $\chi_l/\chi_{\rm c} = 10^6$ to simulate a strong line, with varying ϵ_l (see below). With this setup, the optical depths as seen in the line range from 10^{-2} to 10^6. We use 32 wavelength points to model the full line profile, including wavelengths outside the line for the continuum. We did not require the line to thermalize at the center of the test configurations, this is a typical situation one encounters in a full 3D configurations as the location (or even existence) of the thermalization depths becomes more ambiguous than in the 1D case.

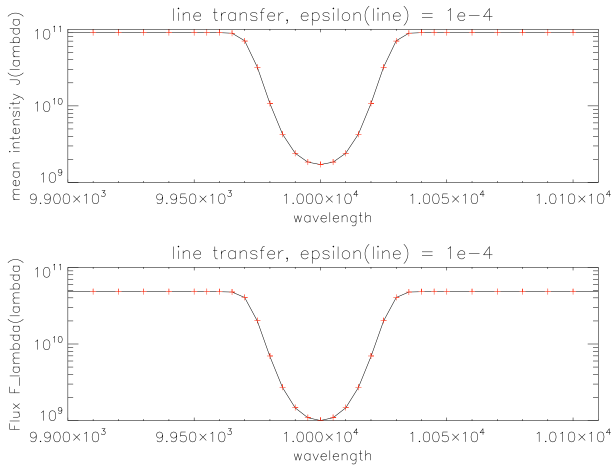

Fig. 3. The mean intensity J and the z component of the radiation flux F at $\tau_{\rm std} = 0$ as function of wavelength. The + symbols are the comparison results with the 1D solver, the full lines the results from the 3D PBC solution. The results are for $\epsilon_l = 10^{-4}$ and constant temperatures.

The slab is mapped onto a Cartesian grid. For the test calculations we use voxel grids with the same number of spatial points in each direction (see below). The solid angle space was discretized in (θ, ϕ) with $n_\theta = n_\phi$ if not stated otherwise. In the following we discuss the results of various tests. In all tests we use the full characteristic method for the 3D RT solution as described above. Unless otherwise stated, the tests were run on parallel computers using 128 CPUs. For the 3D solver we use $n_x = n_y = n_z = 2\times 32 + 1 = 65$ points along each axis. The solid angle space discretization uses $n_\theta = n_\phi = 64$ points.

3.2. Results

We test the accuracy of the 3D PBC solution by comparing it to the results of the 1D code for several line scattering parameters. The 1D solver uses 64 depth points, distributed logarithmically in optical depth. Figures 1–4 show the mean intensities $\bar{J}$ at $\tau_{\rm std} = 0$ and the z component of the emergent flux F as function of wavelength for both the 1D (+ symbols) and the 3D solver.

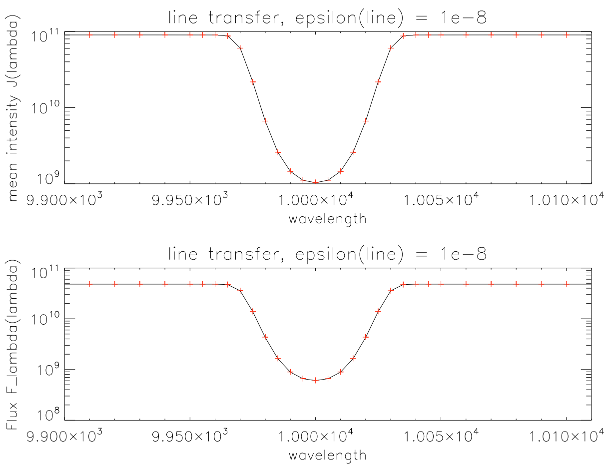

Fig. 4. The mean intensity J and the z component of the radiation flux F at $\tau_{\rm std} = 0$ as function of wavelength. The + symbols are the comparison results with the 1D solver, the full lines the results from the 3D PBC solution. The results are for $\epsilon_l = 10^{-8}$ and constant temperatures.

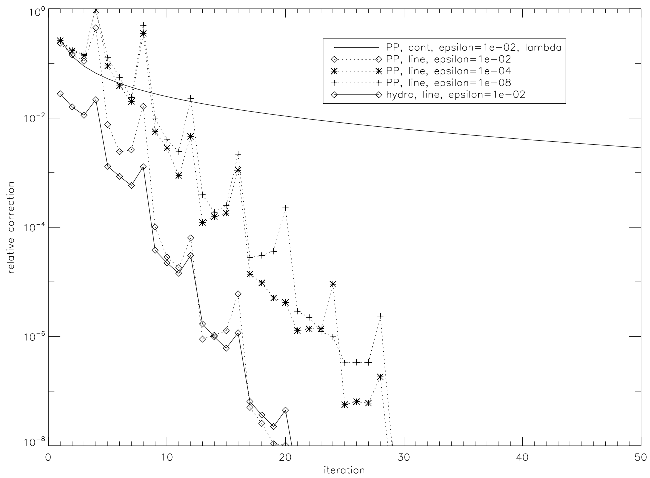

Fig. 5. Convergence rates of the 3D transfer for line transfer with plane-parallel test structures (label "PP") and the 3D hydro structure (label "hydro"). For comparison, the convergence of the Λ iteration for plane-parallel continuum transfer is also shown.

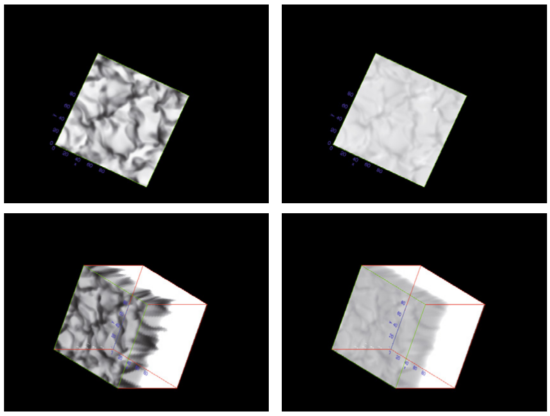

Fig. 6. Visualization of the results for continuum 3D radiation transfer for $\epsilon_c = 1$ (*left panel*) and 10^{-2} (*right panel*). The images are intensities in the directions $\phi = 25$ deg and $\theta = 0$ deg (*top row*) and $\theta = 40$ deg (*bottom row*). An observer would only see the *left face of the cube* (inside the indicated area), the other sides of the cube are shown for clarity and are actually invisible due to the periodic boundary conditions. The scaling of the intensities is the same within each column but different for *the left and right columns*.

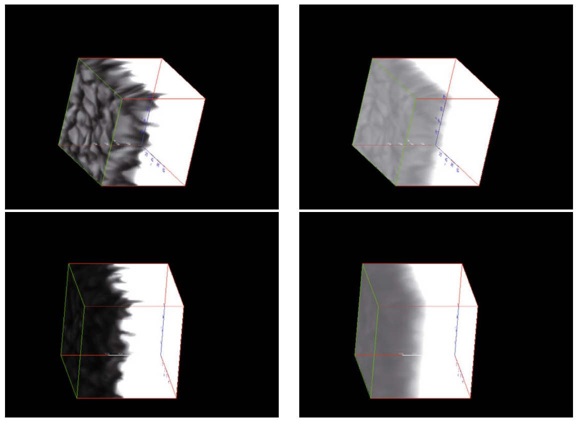

Fig. 7. Same as Fig. 6, but for $\theta = 60$ deg (*top row*) and $\theta = 80$ deg (*bottom row*). The scaling of the intensities is as in Fig. 6. The effect of limb darkening is clearly visible in this figure.

The agreement is excellent for all values of ϵ_l from unity to 10^{-8}, indicating that the 3D code produces an accurate solution even for extreme cases of line scattering. In the case with $\epsilon_l = 10^{-8}$ the continuum processes lead to earler thermalization than the classical approximation $J \propto \epsilon^{1/2}$ as the line strength is limited compared to the continuum. This behavior is the same as in the 1D plane-parallel comparison case. The convergence rate of the line source function (here used together with Ng acceleration) is the same as discussed in Paper II, in the case of $\epsilon_l = 10^{-8}$ the 3D code needed 29 iterations with the nearest-neighbor Λ^* to reach a relative accuracy of 10^{-8} using the simple starting guess $S = B$. The nearest-neighbor Λ^* does allow stopping the iterations earlier than a diagonal (local) Λ^* due to the improved convergence rate (see Paper I). This can easily cut the number of iterations by factors of two or more, even greater savings are possible if the accuracy limit is relaxed.

In addition to the mean intensities, we checked that the flux vectors $\boldsymbol{F}$ have vanishing components in the x and y directions, typically $\max(|F_x|, |F_y|)/|F_z| \leq 10^{-13}$ in all voxels. We stress that this result is the result of the calculations and is not forced by the numerical scheme.

4. Tests with 3D structures

For a test with a computed 3D structure, we obtained an example snapshot structure from Ludwig (Caffau et al. 2007; Wedemeyer et al. 2004) of a radiation-hydrodynamical simulation of convection in the solar atmosphere. The radiation transport calculations were performed with a total of $141 \times 141 \times 151$ grid points in x, y, and z, respectively, for a total of 3 002 031 voxels, the periodic boundary conditions were set in the (horizontal) x, y plane. The transport equation is solved for $n_\theta = 16$ and $n_\phi = 32$ solid angle points, so that a total of about 1.5×10^9 intensities are calculated for each iteration and wavelength point. For the tests described here, we are only using the temperature-density structure of the hydro model and ignore the velocity field for the simple tests presented here. We set the continuum opacity proportional to the density ρ by choosing a rough temperature independent estimate for the Rosseland mean opacity per unit mass of 0.1 cm^2/g and parameterizing the line in the same form as discussed above

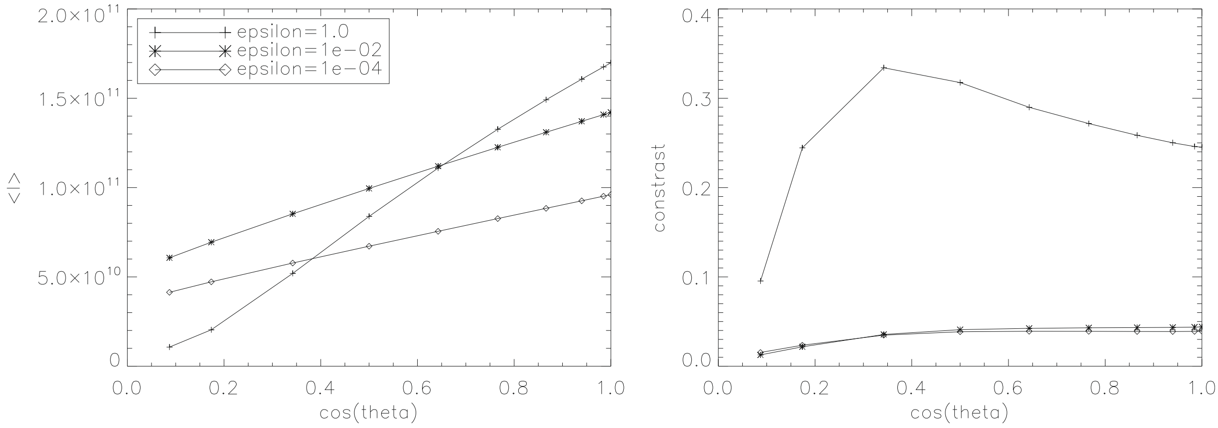

Fig. 8. Limb darkening (*left panel*) and contrast $\sqrt{\langle(I-\langle I\rangle)^2\rangle}/\langle I\rangle$ for 3D continuum transfer with the hydro structure.

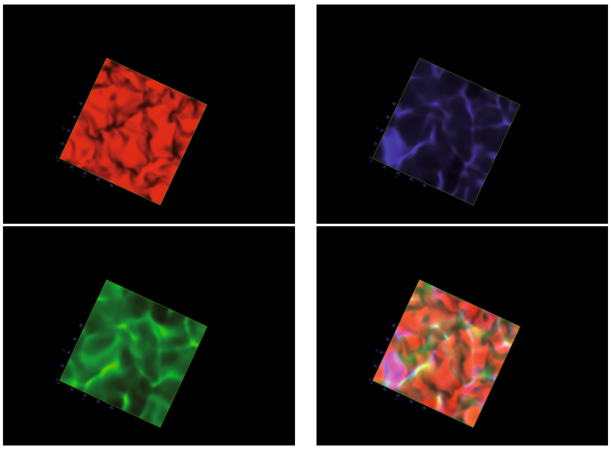

Fig. 9. Visualization of the results for the line 3D radiation transfer with $\epsilon_l = 1$. The images are intensities in the directions $\phi = 25$ deg and $\theta = 0$ deg. The *top left panel* is the image in the continuum, the *top right panel* the image at the line center, the *bottom left panel* the image in the line wing, the *bottom right panel* is a composite image.

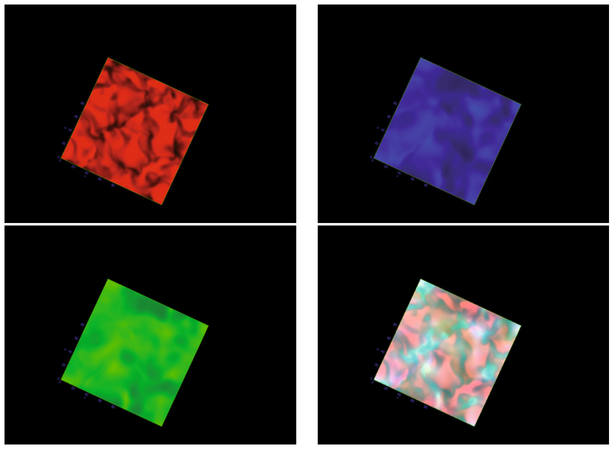

Fig. 10. Visualization of the results for the line 3D radiation transfer with $\epsilon_l = 10^{-4}$. The images are intensities in the directions $\phi = 25$ deg and $\theta = 0$ deg. The *top left panel* is the image in the continuum, the *top right panel* the image at the line center, the *bottom left panel* the image in the line wing, the *bottom right panel* is a composite image.

and in Paper II with a line total (wavelength integrated) opacity of 100 times the local continuum and 32 wavelength points distributed over the full line profile.

4.1. Results

We ran a number of line transfer tests with $\epsilon_l = 1$, 10^{-2} and 10^{-4}. The convergence rates for the two scattering cases are shown in Fig. 5 together with the convergence rates for a small plane parallel test model and the results of the Λ iteration for continuum transfer (for computer time reasons) for a continuum $\epsilon_c = 10^{-2}$. The convergence rate for the plane-parallel tests and the hydro model are remarkably similar, the Λ^* operator delivers very reasonable and practically usable convergence rates.

4.1.1. Images

Figures 6 and 7 show visualizations of the results for 3D continuum transfer. The RT problem was solved for $\epsilon = 1$ (left panels) and 10^{-2} (right panels) and a formal solution with the converged source functions was computed for given viewing angles. The graphs are actual images of the intensities as they would be seen by an external observer different angles. The visible surface is to the left, the "sides" of the computational box could not be seen by an observer and are shown for information only. The effect of scattering on the images is similar to terrestrial fog in that it reduces the contrast of visible features; even moderate scattering of $\epsilon_c = 10^{-2}$ significantly reduces visibility. The limb darkening is also clearly visible in the figures.

Figures 9 to 12 show images generated for the results of the line transfer solution. Three panels show results for individual wavelength (continuum, line wing and line center) and a composite image. The images are significantly different for these wavelengths. The line scattering produces a similar "fog effect" as the scattering in the continuum transfer model, however, the images appear not that different. While one might expect that the line images would look vastly different from the continuum visualization, part of the similarity is due to the fact that they were scaled individually in order to highlight the differences in structure between the wavelengths rather than comparing them on a absolute scale. The composite image (best viewed in color available in the online version of this paper) shows the differences in the visible structures between the different wavelengths.

4.1.2. Limb darkening and contrast

In Fig. 8 we show the limb darkening and contrast for a continuum test case with different values of ϵ. To compute the

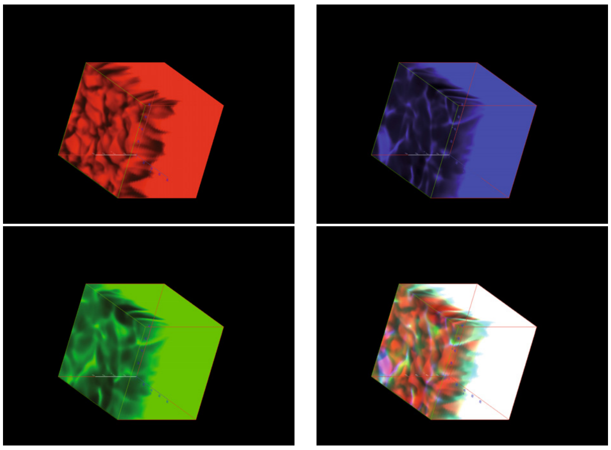

Fig. 11. Visualization of the results for the line 3D radiation transfer with $\epsilon_l = 1$. The images are intensities in the directions $\phi = 25$ deg and $\theta = 50$ deg. The *top left panel* is the image in the continuum, the *top right panel* the image at the line center, the *bottom left panel* the image in the line wing, *the bottom right panel* is a composite image.

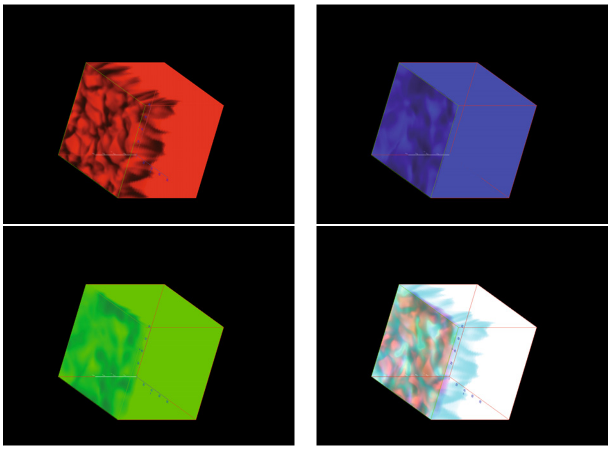

Fig. 12. Visualization of the results for the line 3D radiation transfer with $\epsilon_l = 10^{-4}$. The images are intensities in the directions $\phi = 25$ deg and $\theta = 50$ deg. The *top left panel* is the image in the continuum, the *top right panel* the image at the line center, the *bottom left panel* the image in the line wing, the *bottom right panel* is a composite image.

limb darkening, we calculate the intensity average $\langle I \rangle$ over the visible surface for different values of $\cos(\theta)$ where θ is the angle between the observer and the normal to the surface. We similarly calculate the contrast as $\sqrt{\langle (I - \langle I \rangle)^2 \rangle} / \langle I \rangle$ over the visible surface for different θ. The absolute values of the limb darkening and the contrast depend strongly on ϵ, scattering dramatically reduces the contrast and "flattens" the limb darkening law. Overall, the limb darkening is nearly linear in $\cos(\theta)$, as would be expected from a plane parallel atmosphere with grey temperature structure.

5. Conclusions

Using rather difficult plane parallel test problems, we have shown that our 3D full-characteristics method gives very good results when compared to our well-tested 1D code. The periodic boundary conditions method discussed here is particularly well-suited to 3-D hydrodynamical simulations of convection in stellar atmospheres and in future work we will compare our results to observations as well as to previous calculations. The results for the computed 3D structure show that Λ^* leads also to good convergence for a true 3D structure, with convergence rates that are comparable to the simple test cases (see also Papers I and II).

Acknowledgements. This work was supported in part by by NASA grants NAG5-3505 and NAG5-12127, NSF grants AST-0307323, and AST-0707704, and US DOE Grant DE-FG02-07ER41517, as well as DFG GrK 1351 and SFB 676. Some of the calculations presented here were performed at the Höchstleistungs Rechenzentrum Nord (HLRN); at the NASA's Advanced Supercomputing Division's Project Columbia, at the Hamburger Sternwarte Apple G5 and Delta Opteron clusters financially supported by the DFG and the State of Hamburg; and at the National Energy Research Supercomputer Center (NERSC), which is supported by the Office of Science of the US Department of Energy under Contract No. DE-AC03-76SF00098. We thank all these institutions for a generous allocation of computer time.

References

Asplund, M. 2000, A&A, 359, 755
Asplund, M., Nordlund, Å., Trampedach, R., & Stein, R. F. 1999, A&A, 346, L17
Asplund, M., Nordlund, Å., Trampedach, R., & Stein, R. F. 2000, A&A, 359, 743
Asplund, M., Grevesse, N., & Sauval, A. J. 2005, in Cosmic Abundances as Records of Stellar Evolution and Nucleosynthesis, ed. T. G. Barnes, III, & F. N. Bash, ASP Conf. Ser. 336, 25
Baron, E., & Hauschildt, P. H. 2007, A&A, 468, 255
Basu, S., & Antia, H. M. 2008, Phys. Rep., 457, 217
Caffau, E., Steffen, M., Sbordone, L., Ludwig, H.-G., & Bonifacio, P. 2007, A&A, 473, L9
Grevesse, N., Asplund, M., & Sauval, A. J. 2007, Space Sci. Rev., 130, 105
Hauschildt, P. H., & Baron, E. 2006, A&A, 451, 273
Wedemeyer, S., Freytag, B., Steffen, M., Ludwig, H.-G., & Holweger, H. 2004, A&A, 414, 1121